Nanoscale

PAPER

View Article Online
View Journal

Published on 16 August 2018. Downloaded by University of Illinois - Urbana on 8/23/2018 4:20:31 PM.

Check for updates

Cite this: DOI: 10.1039/c8nr04065f

Carbon dots with induced surface oxidation permits imaging at single-particle level for intracellular studies†

Santosh K. Misra, ‡[a,b] Indrajit Srivastava, ‡[a,b] John S. Khamo, [c] Vishnu V. Krishnamurthy, [c] Dinabandhu Sar,[a,b] Aaron S. Schwartz-Duval,[a,b] Julio A. N. T. Soares,[d] Kai Zhang *[c,e,f] and Dipanjan Pan *[a,b]

Received 19th May 2018,
Accepted 15th August 2018

DOI: 10.1039/c8nr04065f

rsc.li/nanoscale

For robust single particle optical detection, a high sensitivity in photoluminescence (PL) of Carbon Dots (CDs) must be achieved. PL sensitivity can be successfully correlated with their surface chemistry but requires high synthetic control without altering their basic surface properties. Here we describe conditions for the controlled synthesis of CDs that resulted in a PL sensitivity at the single-particle level. We report that a stoichiometric catalyst *N*-methyl morpholine-*N*-oxide (NMMO) can be used as a 'sacrificial' single additive to aid nanoscale surface oxidation. A 24 h NMMO-mediated oxidation increased coverage of oxidized nanoscale surface 3% to 20.9%. NMMO-oxidized CDs (CD-NMMOs) display superior particle brightness, as evidenced by the increase of light absorbance and an enhancement of quantum yield which is characterized by a series of physicochemical and biophysical experiments. We also demonstrate that CD-NMMOs is well suited for intracellular and single-particle imaging.

Introduction

Carbon Dots (CDs) have garnered much attention in recent years owing to their excellent luminescence properties, demonstrating a variety of potential applications in sensing[1–5] and imaging.[6–10] Most of previous work reported CDs emitting in the blue region and only a few demonstrated shifted emissions in the red region.[11–13] CDs with red-shifted emission provide advantages in bio-imaging, because cellular auto-fluorescence generally falls in the blue-green region of the visible spectrum. Studies from our laboratories and others indicated that multiple factors might play roles in influencing the luminescence properties of these agents.[9,14] However, unlike quantum dots, size is not a governing factor for CDs.[15] Due to variation amongst the preparation routes of CDs, it is highly crucial to understand their PL mechanisms so that their optical properties can be tailored based on the application.[16–18] There are at least four possible PL principles proposed, including (i) the quantum confinement effect (π conjugated-domains determined by core; (ii) surface state determined by hybridization of the carbon backbone and the connected functionalities; (iii) the molecular state dictated primarily by fluorescent molecules linked to the surface; and (iv) cross-link enhanced emission (CEE) effect.[18–24] A majority of these mechanisms point to "optical" energy gap, presumably depending upon the surface states arising from the quantum confinement effect. Several groups, including ours, have confirmed that the photoluminescence is tunable and linked to the difference between two energy levels originating from their surface states. However, a variety of surface functional groups, defects and adsorbates are known to be abundant in carbon dots. This complex surface characteristic makes the role of surface states in influencing photoluminescence of CDs poorly defined. In previous reports, photoluminescent carbon dots have been found to behave as electrical dipoles. Their emission originated from the recombination of photo-generated charges on highly abundant 'defect' centers on particle surfaces involving a

[a]Department of Bioengineering, Beckman Institute, Department of Materials Science and Engineering, University of Illinois at Urbana-Champaign, Illinois, USA
[b]Carle Foundation Hospital, 611 West Park Street, Urbana, IL, USA. E-mail: dipanjan@illinois.edu
[c]Department of Biochemistry, University of Illinois at Urbana-Champaign, Urbana, Illinois 61801, USA
[d]Frederick Seitz Materials Research Laboratory Central research facilities, University of Illinois at Urbana-Champaign, Urbana, Illinois, USA
[e]Neuroscience Program, University of Illinois at Urbana-Champaign, Urbana, Illinois 61801, USA
[f]Center for Biophysics and Quantitative Biology, University of Illinois at Urbana-Champaign, Urbana, Illinois, USA. E-mail: kaizkaiz@illinois.edu

†Electronic supplementary information (ESI) available: Hydrodynamic diameter, UV-Vis, ζ-potential, FT-IR, Raman, fluorescence emission measurements of CD and CD-NMMO, chromatographic separation of CD-NMMO, IVIS study, calculation of quantum yield, single-cell image analysis of C32 cells, mass spectra of CD-NMMO fractions and quantum yield table. See DOI: 10.1039/c8nr04065f

‡These authors contributed equally to this work.

Published on 16 August 2018. Downloaded by University of Illinois - Urbana on 8/23/2018 4:20:31 PM.

strong coupling between the electronic transition and collective vibrations of the lattice structure.[19–24] Similarly, relationship between the excitation wavelength and PL emission of the CDs have been investigated and found to be varying with different surface chemistries.[25–30] Although multiple ways of synthesizing such CDs are reported including microwave and hotplate[9,10,15,31–35] arc-discharge,[36] laser ablation[37] electrochemical oxidation,[38] chemical oxidation,[39] ultrasonic synthesis,[40] thermal decomposition,[41] hydrothermal treatment,[42] template based routes,[43] and plasma treatment[44] and synthetic control over wavelength-tuned CDs without changing the reaction composition is not explored well. Methods capable of producing bright CDs that are photo-stable, non-blinking, and background-free for biological imaging using single starting composition are yet to be established. Consequently, these drawbacks restrict their further applications in biological imaging, *e.g.* single-particle imaging. It is significant to detect nanoparticles in their innate biological environment such as in cells, serum or other fluids without altering the physiological conditions. To be precise and free of manipulation during the detection, over the years, single-particle detection systems have become robust, affordable, high-throughput, sensitive in heterogeneous media, and less technically difficult.[45,46]

With the overarching goal to make carbon dots suitable for single-particle biological imaging, there is an urgent need to improve their color tunability. We hypothesized that the introduction of a catalyst in the reaction process may facilitate the generation of oxidizable functional group at the nanoscale surface of nucleating carbon dots. This will consequently lead to electronic changes in the energy gap and, as a result, the coloration might be tuned over a wider range of the spectrum. As-synthesized particles can be fractioned by a polarity-driven chromatographic separation into wavelength-tuned multi-color fraction.

Here we describe conditions for the controlled synthesis of CDs using a stoichiometric ('sacrificial') catalyst as a single additive that aids nanoscale surface oxidation without compromising brightness or stability. Being irreversibly consumed, the sacrificial catalyst is an inexpensive component of the reaction system that allows for regenerating the true catalyst in each cycle. This sacrificial compound is also known as a stoichiometric catalyst since it is consumed in a stoichiometric amount related to the main reactant. In this work, we show that emission wavelength-tuning and subsequent boosting of the quantum yield can be achieved through aerial oxidation of CDs, which is facilitated by sacrificial catalysis. To do this, we report an efficient strategy that synthesizes multi-color and near-infrared CDs using sucrose as the carbon source, aided by a sacrificial catalyst, *N*-methyl morpholine *N*-oxide (NMMO). NMMO is a mild oxidant[47] and acts as a stoichiometric catalyst in several types of oxidation reactions (*e.g.* osmium tetroxide oxidations and the Sharpless asymmetric dihydroxylation reaction). We hypothesized that NMMO will help expedite the hydrothermal synthesis of multi-colour CD-NMMOs (Fig. 1A) and trigger facile oxidation of the nanoscale surface increasing gradually with the time of reaction and verified qualitatively by consistent loss of sacrificial catalyst, *N*-methyl morpholine *N*-oxide (NMMO) peak in mass spectrum at 118.0875 (Fig. 1B–E; Spectra S1–S5†). We demonstrate that introduction of a catalyst in the reaction mixture effectively triggers *in situ* aerial oxidation with progressive luminescence tuning, presumably leading to electronic changes in the energy gap and consequently resulting in a colour tuning. Our results for the first time demonstrated that NMMO-facilitated aerial oxidation led to highly luminescent multi-colour CDs that are ideally suited for single particle intracellular imaging.

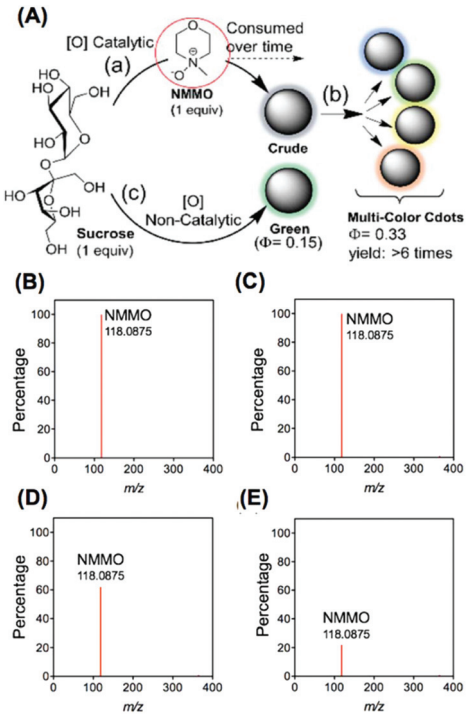

Fig. 1 CD-NMMO for producing multicolor carbon dots using 'sacrificial' catalysis. (A) Schematic representation of the process of preparing multi-color CDs by using NMMO as a stoichiometric catalyst mixed with sucrose. Nucleation of crude particles by catalytic process indicates irreversible consumption of the catalyst over a reaction time of 24 h. Mass spectra of CD-NMMO oxidized for (B) 1 h, (C) 2 h, (D) 8 h and (E) 24 h.

Experimental methods

Materials

Unless otherwise stated, all chemicals were purchased from Aldrich Chemical Co. (St Louis, MO) and used as received.

Dynamic light scattering

The hydrodynamic size distribution (intensity average) of the nanoparticles was determined by dynamic light scattering (DLS) measurements on Malvern Zetasizer ZS90 instrument (Malvern Instruments Ltd, United Kingdom) at a fixed angle of 90°. A 20 μL of particle suspension was mixed with 980 μL of nanopure water to run the samples in DLS machine. A photomultiplier aperture of 400 nm was used and the incident laser

 This journal is © The Royal Society of Chemistry 2018

Published on 16 August 2018. Downloaded by University of Illinois - Urbana on 8/23/2018 4:20:31 PM.

power was so adjusted to obtain a photon counting rate between 200 and 300 kcps. Particle diameters were determined based on measurements whose measured and calculated baselines of the intensity autocorrelation function were within 0.1%. All measurements were carried out in a triplicate of fifteen consecutive measurements.

Zeta potential measurements

Zeta potential (ζ) values were determined using a Malvern Zetasizer (Malvern Instruments Ltd, United Kingdom) of Nano series. The experiments were performed at 25 °C and pH 7 at the light scattering mode in the phase analysis light scattering (PALS) mode following solution equilibration at 25 °C. Calculation of ζ from the measured nanoparticle electrophoretic mobility (μ) employed the Smoluchowski equation: $\mu = \varepsilon\zeta/\eta$ where ε and η are the dielectric constant and the absolute viscosity of the medium, respectively. Measurements of ζ were reproducible within ±4 mV of the mean value, given by 3 determinations of 15 data accumulations.

Column chromatography

Different coloured fractions of as-prepared CD-NMMOs were critically separated using a silica gel (230–400 mesh size) by column chromatography technique using a mixture of ethyl acetate and ethanol. For complete separation of different coloured fractions, it took 3 days due to slow flow rate used so as to avoid cross-contamination amongst CDs with different polarities.

UV-Vis and fluorescence measurements

Ultraviolet-visible (UV-Vis) absorbance of CDs was recorded on GENESYSTM 10S UV-Vis Spectrophotometer (Thermo Scientific, MA, USA). Absorbance spectra were collected at an interval of 1 nm scanning from 250–800 nm. The emission spectra of fluorescence measurements were obtained through TECAN Infinite F200 PRO.

Raman and FT-IR measurements

An aqueous suspension of the nanoparticles was dried onto a MirrIR IR-reflective glass slide (Kevley Technologies, Chesterland, Ohio, USA) for Fourier Transform Infrared (FT-IR) measurements using a Nicolet Nexus 670 FT-IR (Fredrick Seitz Material Research Laboratories (FSMRL), Urbana, Illinois, USA). For each measurement 100 × 100 μm images were collected at 1 cm^{-1} spectral resolution with 64 scans per pixel and a 25 × 25 μm pixel size and individual spectra were corrected for atmospheric contributions. Raman spectra were recorded using Nanophoton Raman 11.

Mass spectroscopy

CD-NMMO samples oxidized for different times were analyzed by Mass spectroscopy using electrospray ionization mass spectrometry (ESI-MS) technique.

X-ray photoelectron spectroscopy

X-ray photoelectron spectroscopy (XPS) measurements for CDs was obtained on a thick vacuum dried layer of the NPs applied on the glass surface using Physical Electronics PHI 5400 spectrometer with Al Kα (1486.6 eV) radiation. The spectrum was referenced to the adventitious C 1s feature at 285.0 eV.

Fluorescence imaging

Fluorescence measurements were performed at the Illinois Sustainable Technology Center. Fluorescence excitation–emission measurements (EEM) were performed with a Horiba Aqualog scanning spectrophotometer/spectrofluorometer. The samples were scanned over an excitation range of 240 nm to 700 nm and an emission range of 246 nm to 828 nm. The integration time was set at 0.1 seconds and the wavelength scan increments were set for 3 and 5 nm, excitation and emission, respectively. All samples were blank subtracted with data obtained from analysis of a deionized water blank. Post-processing of the fluorescence data included inner-filtering correction with data obtained by simultaneous absorbance measurements and Rayleigh masking of signals produced as a result of light scattering of water. In addition, all emission intensities were normalized to a 1 mg L^{-1} quinine sulfate solution that was analysed prior to each assay.

PL lifetime experiments

PL lifetime experiments were performed for CDs at an excitation wavelength of 390 nm, and at 510 nm for CD-NMMO-R with emission range of 400 nm–700 nm and 525 nm–700 nm, respectively. A single-photon-counting setup at MRL, UIUC facility was used. The experiment was performed with the lifetime of emitting states with single photon sensitivity and <1 ns temporal resolution at a temperature of 273 K. A particle concentration of 1 mg mL^{-1} was used for the experiment in a volume of 200 μL loaded in a quartz cuvette.

In Vivo Imaging System (IVIS) imaging

Fluorescence imaging study was performed using Xenogen IVIS system, wherein serially diluted samples of CD 24 h and CD NMMO 24 h were filled in a Corning® 384 well optical imaging flat clear bottom black polystyrene TC-treated microplates.

Relative quantum yield calculations

Quinine sulfate in 0.1 M H_2SO_4 solution was used as a standard for CD, CD-NMMO-B and CD-NMMO-G, where fluorescein isothiocynate, FITC (0.1 mg ml^{-1} in water) was used as a standard for CD-NMMO-Y and CD-NMMO-R. The quantum yield of blue fraction, green fraction, yellow fraction and red fraction was calculated using the following formula:

$$\Phi = \Phi_R \times \frac{I}{I_R} \times \frac{A_R}{A} \times \frac{\mu}{\mu_R}$$

where Φ is the quantum yield, I is the measured integrated emission intensity, μ is the refractive index, and A is the absorbance. The subscript R refers to the standard, quinine sulfate (data were calculated according to the above equation and listed in Table S1†). Excitation wavelength when using quinine sulfate as standard was 365 nm, where for FITC it was 470 nm.

Published on 16 August 2018. Downloaded by University of Illinois - Urbana on 8/23/2018 4:20:31 PM.

Single-particle fluorescence microscopy

Objective-based total internal reflection fluorescence microscopy (TIRFM) was used for single-particle imaging. A continuous wavelength (488 nm, Spectral physics) laser was used as the light source. An inverted microscope (IX73) equipped with a 100× oil immersion objective (Olympus, PlanApo, 100×, N.A. 1.49, oil immersion) was used. The laser beam was then expanded, collimated to about 35 mm, and directed into the microscope by 400 mm lens (Thorlabs LA1725A). The incident light was directed through the objective *via* an exciter (FF01-482/563-25, Semrock) and a dual-band dichroic filter (Di01-R488/561-25×36, Semrock). The mean excitation power before the objective is about 1.5 mW cm^{-2}. The luminescence photons from individual CDs were collected by the same objective, passing an emitter (FF01-523/610-25, Semrock) and captured by an Electron Multiplying Charge Coupled Device (EMCCD) camera (iXon U797, Andor. Technology) The emission filter was designed to have a spectral cut off at 500–548 nm, covering the central wavelength of CDs emission at 500 nm. Thus, experimental observations of emission intensity were not affected by potential spectral diffusion of ±10 nm. The sample coverslip was secured onto a 2-D stage. Individual nanoparticles were located by raster scanning the stage. An exposure time of 100 ms was used. At least ten time-stamped image stacks, each of which consists of 600 frames, were taken for each type of particle.

Intracellular imaging of CD-NMMOs with epi-fluorescence microscopy

An *epi*-illumination inverted fluorescence microscope (Leica DMI8) equipped with a 100× objective (HCX PL FLUOTAR 100×/1.30 oil) and a light-emitting diode illuminator (SOLA SE II 365) was used to image CDs in fixed cells. Red fluorescence was detected using the TX2 filter cube (Leica, excitation filter 560/40, dichroic mirror 595, and emission filter 645/75). Green fluorescence was detected using the GFP filter cube (Leica, excitation filter 472/30, dichroic mirror 495, and emission filter 520/35). Exposure time for both fluorescence channel was 200 ms.

Image analysis for single-particle imaging

All analysis for single-particle imaging was performed with a custom-written software in MATLAB. For each frame, a 7 × 7-pixel area surrounding each individual fluorescent spot was identified. The background level was calculated by averaging the intensity of the peripheral pixels excluding the central spot. The intensity of each spot was calculated by averaging all intensities from each pixel within the central spot. The net intensity of each spot was calculated by subtracting the background level from that of the central spot. The number of photons was calculated by following a formula provided by the vendor.

$$\text{Photons} = \frac{(\text{electrical count} - \text{bias offset}) \times \text{preamp}}{\text{EM gain} \times \text{QE}}$$

Intracellular image analysis for CD-NMMOs

The region of interest (ROI) Manager plugin from FIJI was used to analyze the correlation of fluorescence intensities for CD-NMMOs in C32 cells. A snapshot of each field of view was acquired in three channels (TX2, GFP, and Phase contrast). Manual selection of the cell profile was used to enclose each cellular area. An ROI with no cells were selected as the background. The average fluorescence intensity in each ROI was measured from the plugin. The fluorescence intensity of each cell was calculated by subtracting the background level from that of each cell. More than 50 cells were analysed for each condition.

Imaging CD-NMMO fraction with epi-fluorescence microscopy

C32 cells were seeded into a multi-cavity PDMS chamber (cavity diameter = 5 mm) placed on top of a coverslip 24 hours before treatment. Prior to imaging, cells were incubated with each CD fraction (one per cavity) for 15 min at 37 °C, 5% CO_2, followed by a single wash and submersion with DPBS. Live cells were imaged using an inverted *epi*-illumination fluorescence microscope (Leica DMI8) equipped with a 100× objective (HCX PL FLUOTAR 100×/1.30 oil) and a light-emitting diode illuminator (SOLA SE II 365). Red fluorescence was detected using the Y5 filter cube (Leica, excitation filter 620/60, dichroic mirror 660, and emission filter 700/75) with an exposure time of 600 ms. Yellow fluorescence was detected using the TX2 filter cube (Leica, excitation filter 560/40, dichroic mirror 595, and emission filter 645/75) with an exposure time of 300 ms. Green fluorescence was detected using the GFP filter cube (Leica, excitation filter 472/30, dichroic mirror 495, and emission filter 520/35) with an exposure time of 200 ms. Blue fluorescence was detected using the DAPI filter cube (Leica, excitation filter 350/50, dichroic mirror 400, and emission filter 460/50) with an exposure time of 100 ms.

Results and discussion

In a non-catalytic process, pristine carbon nanoparticles, referred to as CDs, were prepared hydrothermally from sucrose. The average hydrodynamic diameter of CDs prepared at 24 h time point was 20 ± 5 nm with a negative electrophoretic (zeta) potential of −40 ± 6 mV (Fig. S1†). For the catalytic process, the same reaction condition was used except for the addition of NMMO in a stoichiometric amount with respect to that of CD (1 : 1 wt%). Progressive oxidation of this stoichiometric mixture of sucrose and NMMO was carried out for 1, 2, 8, and 24 h, producing CD-NMMO.

Mass spectrometry (MS) studies (Fig. 1B–E; Spectra S1–S4†) showed that NMMO was irreversibly consumed as the reaction time was increased from 1 h to 24 h, confirming its role as a sacrificial catalyst. The chemical integrity of obtained CD-NMMOs was confirmed using dynamic light scattering (DLS), UV-Vis spectroscopy, electrophoretic potential (Zeta), X-Ray photoelectron spectroscopy (XPS) and mass spec-

 This journal is © The Royal Society of Chemistry 2018

Published on 16 August 2018. Downloaded by University of Illinois - Urbana on 8/23/2018 4:20:31 PM.

trometry (MS). DLS of CD-NMMOs prepared after 1 h of oxidation with NMMO resulted in an average hydrodynamic particle diameter of ~800 nm (Fig. S2†), indicating incomplete nucleation to CD-NMMOs. However, the average diameter reduced to 15 ± 5 nm as we increased the time of oxidation to 24 h (Fig. S3†). UV-Vis profiles for these small CD-NMMOs showed characteristic peaks at 280 nm and 320 nm, due to π–π* transition of the conjugated C=C bond of carbonaceous core and n–π* transition of the C=O bond present on the surface in form of oxidized functional groups, *e.g.* –COOH. It was interesting to note that the absorbance of the CD-NMMOs increased for lengthened oxidation time, indicating a role of oxidized surfaces in enhancing their absorption efficiency (Fig. S4†). Electrophoretic mobility studies for various CD-NMMOs revealed that zeta potentials became more negative with an increase of oxidation time, likely due to an increased abundance of carboxylic and hydroxyl groups (Fig. S5†).

Surface oxidations on CD-NMMOs were quantified by a gradual appearance of a higher percentage of oxidized surface chemistries in XPS analysis de-convolving the C 1s spectra and extracting the percentage of –COOH group in both CDs and CD-NMMOs (Fig. 2A and B). CDs generated from a non-catalytic process has only ~3% of surface –COOH group (Fig. 2C), whose percentage increases to ~21% in the 24 h-oxidation CD-NMMOs (Fig. 2D). This result suggests that NMMO catalyzed the oxidation of the $–CH_2$ and –CH–OH groups on the surface of CDs to produce –COOH group by complete and partial oxidation, respectively (Table 1) and were supported by elemental composition of the O 1s spectra of CD-NMMO and CDs (Table 2). 2D-emission plots also confirm that emission peak of CD-NMMOs shifted to longer wavelength in comparison to CDs (Fig. 2E and F).

To further analyze the distinct features of surface functional groups in CDs and CD-NMMOs, we performed optical spectroscopic analysis for both samples. Fourier-transform infrared (FT-IR) spectroscopy showed an increased absorption of C=O at 1500 cm^{-1} in CD-NMMOs compared with CDs (Fig. S6†). There was no change in the vibration energy, suggesting a consumptive catalytic role of NMMO, *i.e.*, NMMO does not integrate into CDs as such but presumably its byproducts do after being produced during sucrose oxidation. In representational Raman spectrum of carbon nanoparticles (Fig. S7†), the presence of D and G modes are found to be characteristic where the G peak originates at a higher wavenumber than the D peak. The D peak is generally corresponding to the vibrations of disordered sp^2-hybridized carbon atoms and appears in carbon particle samples with high structural defects. The G peak refers to the tangential stretching vibrations of the C–C bond.[48]

The intensity ratio of these signature Raman peaks (I_D/I_G) can be used to study the degree of surface defect and the relative ratio of carbon atoms within particles and at the surface. A higher (I_D/I_G) ratio represents increasing surface defects and decreasing sp^2 carbons. These both conditions can be corroborated with surface oxidation where sp^2 carbon involves in oxidation can introduce surface defects. Raman spectroscopy study on CD's revealed signature defect and graphene bands at 1269 and 1552 cm^{-1} which were shifted to 1246 and 1521 cm^{-1}, respectively in case of CD-NMMOs. This change in Raman shift position of CD in CD-NMMO indicates the varying surface energies. Raman scattering pattern also featured a consumptive catalytic role of NMMO with change in the G and D band ratios, which was accompanied by a slight decrease in the graphitic nature of CD-NMMOs (Fig. S7†).

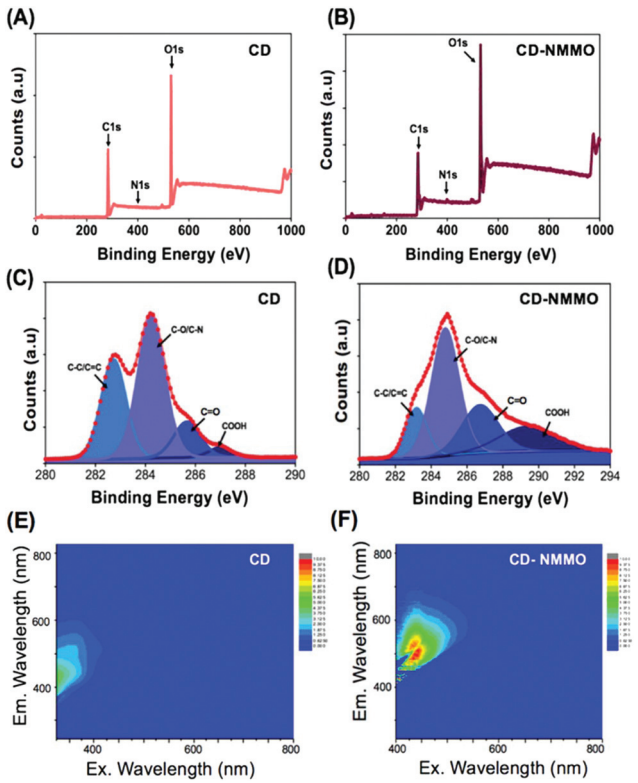

Fig. 2 X-ray photoelectron spectroscopy of (A) CD oxidized for 24 h and (B) CD oxidized for 24 h in presence of NMMO. C 1s de-convolved X-ray photoelectron spectra of (C) CD oxidized for 24 h and (D) CD oxidized for 24 h in presence of NMMO. Excitation and Emission (EMM) fluorescence images of (E) CD-NMMO oxidized for 24 h and (F) CD oxidized for 24 h, both at a concentration of 0.5 mg ml^{-1}.

Table 1 Representative XPS data analyses of the C 1s spectra for CD-NMMO and CDs

Sample	C–C; C=C	C–N; C–O	C=O	COOH
CD-NMMO	47.6%	19.87%	11.62%	20.91%
CD	51.4%	32.88%	12.47%	3.2%

Table 2 Elemental composition of the O 1s spectra

Sample	C (%)	N (%)	O (%)	O/C (%)
CD-NMMO	61.06	1.28	37.67	0.61
CD	67.49	—	32.5	0.48

Published on 16 August 2018. Downloaded by University of Illinois - Urbana on 8/23/2018 4:20:31 PM.

Similarly, high surface oxidation could cause more defects in graphitic patterns of CD-NMMOs compared to CDs and in turn induce a decrease in the graphitic band.

Intrinsic photoluminescence of CDs is important to make them traceable for cellular imaging studies and following up their fate post cell internalization. To evaluate the emission properties of CD-NMMOs, spectroscopic measurements were performed. When excited by 365 nm UV light, non-catalytic CDs displayed two emission peaks around 450 nm and 500 nm (Fig. S8A†), whereas CD-NMMOs showed extra, red-shifted emission around 550 nm and 625 nm and multiple shoulders in the 675–725 nm range (Fig. S8B†). Emission spectra with multiple peaks indicate the possibility of either one species with multiple emissions or multiple species of single emission present in the suspension.

CD-NMMO (24 h) was subjected to silica-gel column separation to produce four different fractions of particles based on their surface polarity. Column loaded with CD-NMMO was eluted with ethyl acetate (100%) followed by ethyl acetate : ethanol (80 : 20 volume ratio). Fractions were collected on the basis of their polarity with CD-NMMO-B being the least polar, getting separated first, and CD-NMMO-R being most polar gets separated last.[27] Collected fractions were allowed to dry and re-suspended in water. The hydrodynamic diameters of CD-NMMO-B, CD-NMMO-G, CD-NMMO-Y and CD-NMMO-R fractions were found to be sub-20 nm. CD-NMMO-B and CD-NMMO-G were smallest and biggest in size, respectively (Fig. 3A). The anhydrous state morphology of each fraction was acquired by transmission electron microscopy, where a representative micrograph of CD-NMMO-R showed a size of 15 ± 5 nm with a spheroidal morphology (Fig. 3B). Collected fractions were checked for UV absorption with no significant change in band position at ~360 and ~500 nm (Fig. S9†). Each of these fractions were referred to as CD-NMMO-B, CD-NMMO-G, CD-NMMO-Y, and CD-NMMO-R, respectively based on their color under UV lamp (362 nm) (Fig. 3C). The photoluminescence spectra at different excitation wavelengths of 370 nm, 410 nm, 470 nm and 510 nm for the blue, green, yellow and red fractions, respectively showed distinct emissions ranging from 400 to 750 nm (Fig. 3D).

To study the photo-responses, a time-resolved photoluminescence study was performed on CD-NMMO and its separated fractions. The photoluminescence decay curve for CD-NMMO mixture and the separated fractions were fitted by using a bi-exponential function (Fig. 4). All fractions showed a PL lifetime between 2.6–3.2 ns owing to similar surface states (Table S1†). Furthermore, the red fraction showed a slightly longer half-life when excited at 510 nm (~5 ns) than that excited at 390 nm (~3 ns). Possibly a higher excitation wavelength was allowing it to stay in unique excited state for a longer duration on 510 nm excitation compared to distinct excited state obtained for 390 nm excitation. Stability of spec-

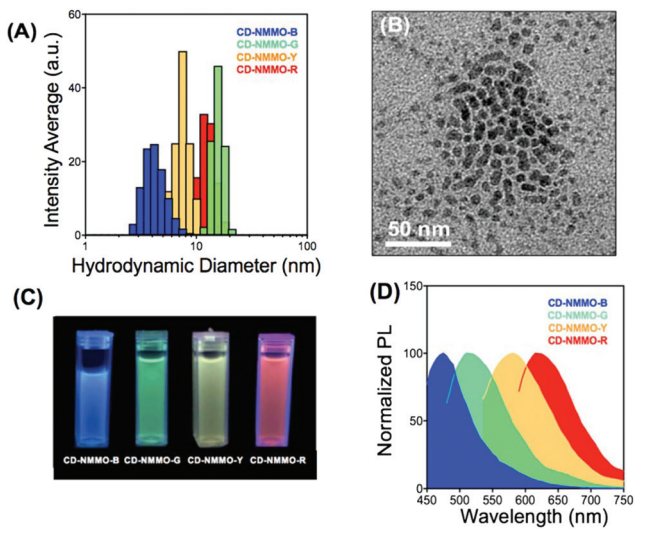

Fig. 3 Size and morphological characterization of CD-NMMO fractions. (A) Distinguishable hydrodynamic diameter of multi-color CDs and (B) a representative TEM image of CD-NMMO from red fraction. Optical characterization of CD-NMMOs. Column chromatographically separated fractions under (C) UV light of 365 nm, (D) emission property with varying λ_{em} for different fractions ranging from blue, green, yellow to red, excited at 370 nm, 410 nm, 470 nm and 520 nm, respectively.

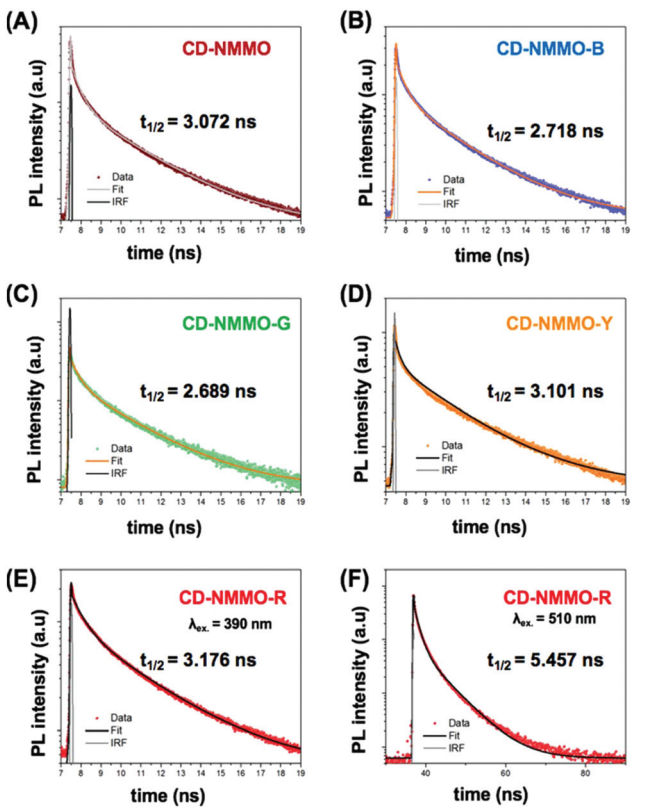

Fig. 4 Time resolved photoluminescence (TRPL) spectra of (A) CD-NMMO mixture along with the column separated components, (B) blue fraction, (C) green fraction, (D) yellow fraction and (E) red fraction measured at $\lambda_{excitation}$ 390 nm and (F) red fraction measured at $\lambda_{excitation}$ 510 nm. Corresponding half-lives and chi-squared values have been provided (Table S1†).

This journal is © The Royal Society of Chemistry 2018

Published on 16 August 2018. Downloaded by University of Illinois - Urbana on 8/23/2018 4:20:31 PM.

tral properties under constant photon exposure provides information on its usability for imaging applications. A distinctly high wavelength emission (λ_{em} = 720 nm) and rather less significant change from serial dilution effects (1 : 0–1 : 8) were also achieved by CD-NMMO particles compared to CDs under IVIS study (Fig. S10A†). Calculation of average radiant efficiency showed significantly low dilution effect on CD-NMMO particles (Fig. S10B†).

To determine the photo luminescent quantum yield (QY) of each fraction, we used quinine sulfate solution as a reference for CD, CD-NMMO-B, CD-NMMO-G, CD-NMMO-Y, and CD-NMMO-R. In each measurement, the absorbance, integrated emission intensity, and refractive index of reference and samples were determined. Compared with CDs prepared without the sacrificial catalyst (Φ = 0.16), NMMO treatments increased the quantum yield: CD-NMMO-B (Φ = 0.21), CD-NMMO-G (Φ = 0.26), CD-NMMO-Y (Φ = 0.236), and CD-NMMO-R (Φ = 0.244) (Table S2†). These results make CD-NMMOs promising candidates for single-particle analysis, where individual particle emission intensity with minimal dilution effect (local solvent molecule effect) would be the most important feature.

Because the CD-NMMOs have broad excitation spectrum from 260 nm to 500 nm (Fig. S3†), we reason that commonly used single-molecule fluorescence microscope can be used to characterize the photophysical properties of single carbon dots. The excitation wavelength 488 nm was chosen because it was sufficient to excite all nanoparticles (Fig. S8†). In particular, we cover emission from 500 nm to 650 nm because extra fluorescence peaks were observed in CD-NMMOs compared with non-catalytic CDs. For single-particle imaging, we deposited 40 μL of solutions containing CDs or CD-NMMOs to each cavity (1 mm in diameter) of a polydimethylsiloxane (PDMS) chamber (Fig. 5A). Such a device allows for detection

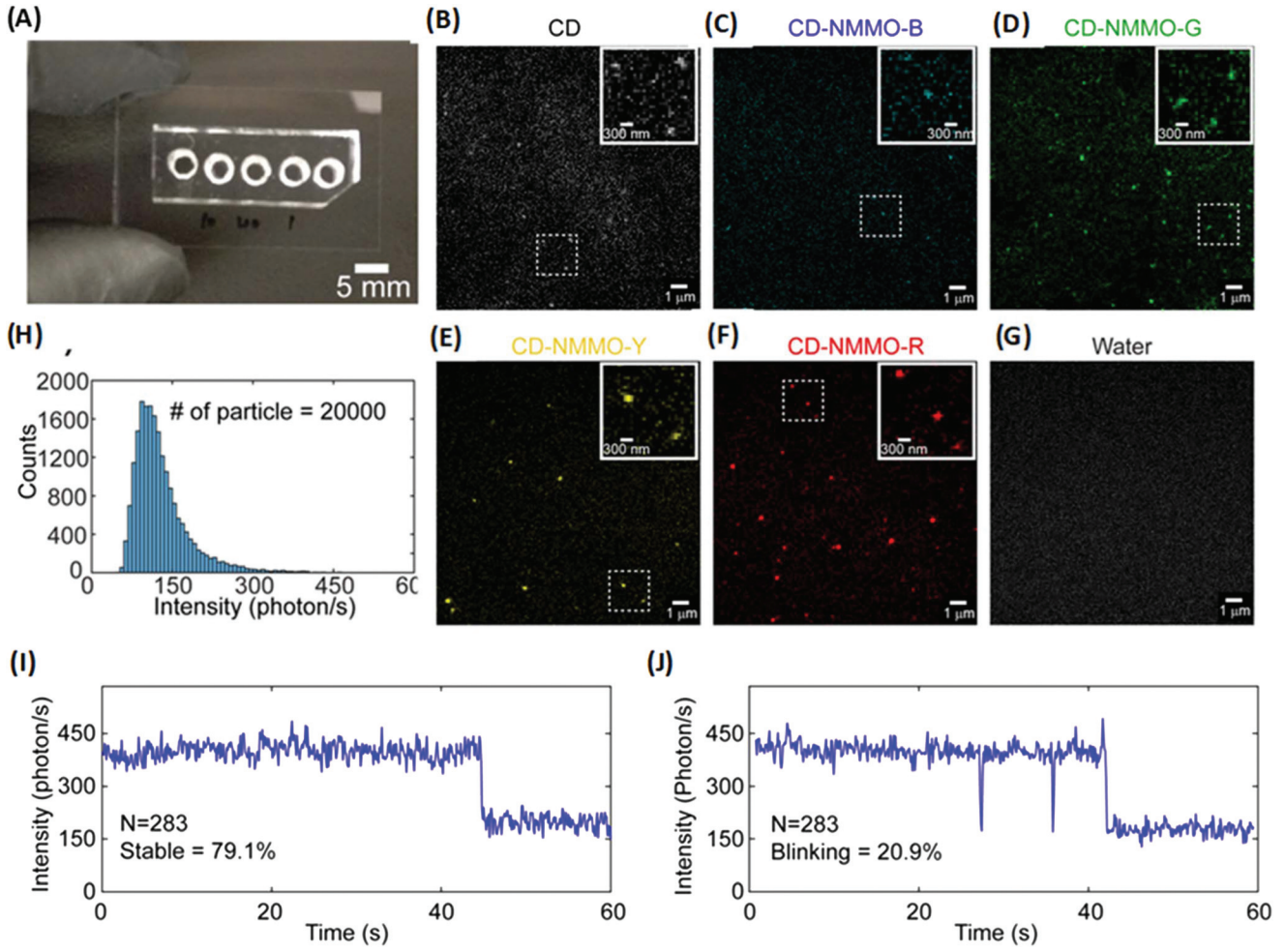

Fig. 5 Single particle imaging of CD-NMMO and its fractions CD-NMMO-B, CD-NMMO-G, CD-NMMO-Y, and CD-NMMO-R. (A) A home-made micro-cavity device used in single-particle imaging. Up to five samples can be imaged on the same coverslip. Representative single-particle emission images of (B) CD-NMMO, (C) CD-NMMO-B, (D) CD-NMMO-Y, (E) CD-NMMO-G and (F) CD-NMMO-R as captured by an EMCCD camera. Inset: Individual particles form diffraction-limited images and (G) a snapshot of a sample without CDs (control). (H) A histogram of emission intensity from 20 000 single CD-NMMOs. (I, J) Representative intensity trajectories from single CD-NMMOs, which show a typical single-step photo bleaching. Out of 283 CD-NMMOs, approximately 80% displayed stable trajectory (I) and 20% displayed transient blinking (J).

Published on 16 August 2018. Downloaded by University of Illinois - Urbana on 8/23/2018 4:20:31 PM.

of multiple types of particles on the same substrate. The sample was diluted in water so that 500 particles were detected within an 80 μm × 80 μm field of view. A home-built total-internal-reflection-fluorescence (TIRF) microscope equipped with a 488 nm, a 100× oil-immersion objective, and an electron multiplying Charge-Coupled Device (EMCCD) was used to image individual particles. Individual particles were detected as bright diffraction-limited spots (Fig. 5B). The excitation power was 1.5 mW at the back aperture of the objective. Similar images were obtained from CD-NMMO-B (Fig. 5C), CD-NMMO-Y (Fig. 5D), CD-NMMO-G (Fig. 5E) and CD-NMMO-R (Fig. 5F) samples. A control with solvent (water) alone was measured to confirm that the signal was indeed resulting from the carbon dots. As shown in the Fig. 5G, there are significantly less, if any, particles that can be detected for this negative control. Ten time-stamped images of 600 frames were then taken for each field of view. With a dynamic frame transfer mode turned on, transfer time between sequential frames is about 1 ms, which makes the total trajectory time slightly longer than 60 s with a 100 ms exposure time.

The intensity of each particle was analyzed by a Matlab script that allows for semi-automatic detection of bright spots.[49] Because CD-NMMOs' emission properties depend on molecules on their surface, we did not apply any chemical-conjugation strategy to immobilize these particles on the glass surface. This would not affect measurement of the brightness at the single-particle level because the evanescent field used in TIRF microscopy only excites particles localized within 200 nm distance from the surface. For particles diffusing away from the focus during image acquisition, their intensities were then calculated by averaging all frames over their prior surface-dwelling time. The representative distribution of individual CD-NMMO particle intensity is shown in Fig. 5H. For the majority of nanoparticles, we observe a flat emission trajectory with minimal photo-blinking (Fig. 5I). To determine the photostability and photo blinking of individual CD-NMMOs, images were collected using an acquisition time of 600 frames (60 s). This helped us detect a single-step bleaching behavior. Results from 283 particles indicated 80% displayed flat trajectories (Fig. 5I) and 20% displayed transient blinking lasting less than 1 s (Fig. 5J).

To quantitatively determine the brightness of particles in each fraction (CD-NMMO-B, CD-NMMO-G, CD-NMMO-Y and CD-NMMO-R), we performed single-particle imaging for each fraction (Fig. 6). Within the emission spectrum window (500–550 nm & 585–635 nm), the yellow and red fractions appeared brighter than the blue and green fractions as well as CD alone. This result confirmed that particles in the yellow and red fractions exhibit significant red-shift in their emission peak and enhancement of single-particle brightness compared with pristine CDs.

Intracellular emission features of CD-NMMOs were investigated in C32 mammalian cells (model human melanoma cells). Cells were incubated with CD-NMMOs (1 mg mL^{-1}) for 4 h before fixation with 4% paraformaldehyde. Cells incubated with CDs or with no particles were used as negative controls

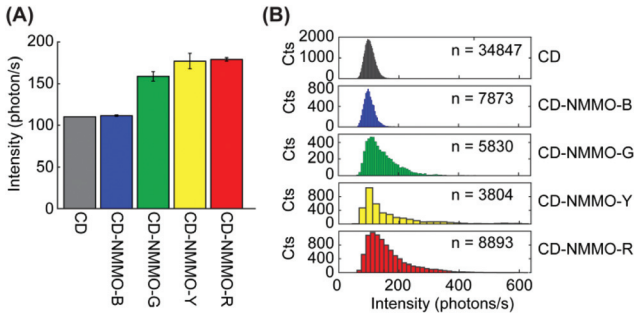

Fig. 6 Single particle analysis of CD-NMMO fractions. (A) Single-particle analysis of the brightness of each fraction of CD-NMMO and CD alone. (B) The histogram shows intensity distribution of each fraction of particles. Green, yellow, and red fractions show extended peak shift to the right (brighter). This extension indicates appearance of particles with enhanced fluorescence at single particle level.

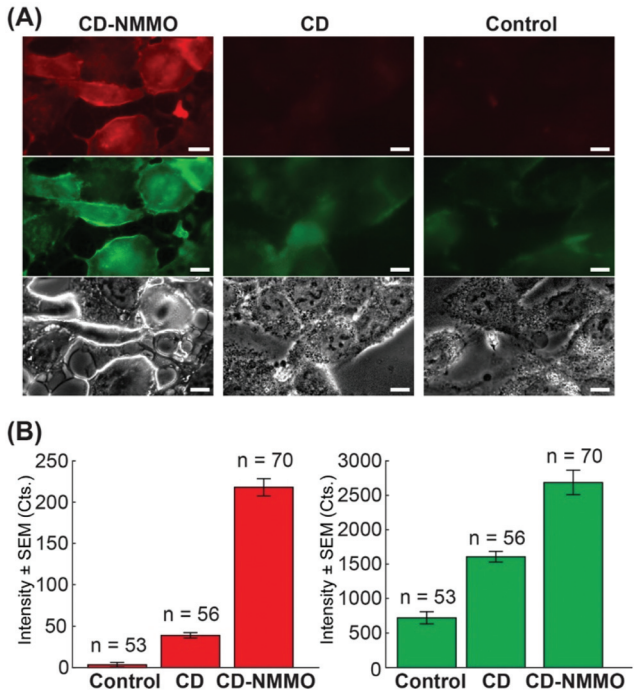

Fig. 7 Intracellular single-particle imaging of CD-NMMOs compared with CDs. (A) Fluorescence measurement of C32 cells incubated with CD-NMMO (left), CD (middle), and no particles (right). Cells were incubated with or without particles, fixed on coverslip, and imaged with epi-fluorescence microscopy. The dynamic range for each of the three images in the red (top) and green (middle) channels were identical. CD-NMMO incubated cells show significantly brighter images. (B) Quantification of cell brightness in both red (left) and green (right) fluorescence channels. The base level from control may arise from auto fluorescence of cells. The number of cells (*n*) analyzed in each condition was marked above each bar. For the green channel, the excitation wavelength was 450–490 nm and emission wavelength was 500–550 nm. For red channel, the excitation wavelength was 540–580 nm and emission wavelength was 600–675 nm.

(Fig. 7). Cells incubated with CD-NMMO showed strongest emission in both green and red channels (Fig. 7A and Fig. S11†), indicating the presence of CD-NMMO's with

This journal is © The Royal Society of Chemistry 2018

Published on 16 August 2018. Downloaded by University of Illinois - Urbana on 8/23/2018 4:20:31 PM.

different wavelength emissions. For the green channel, the excitation wavelength was 450–490 nm and emission wavelength was 500–550 nm. For red channel, the excitation wavelength was 540–580 nm and emission wavelength was 600–675 nm. Considering the relative strong cellular auto-fluorescence in the green channel, we believe red channel is a better choice for intracellular imaging with CD-NMMOs (Fig. 7B). We also examined the intracellular imaging capacity for each of the fractions of CD-NMMOs. Cells were prepared with the same protocol as mentioned above. We found equally efficient CD-NMMO-B, CD-NMMO-G, CD-NMMO-Y, and CD-NMMO-R fractions in DAPI, GFP, TX2 and Y5 regions, respectively (Fig. S12†). Because autofluorescence raises the baseline of fluorescence within the intracellular environment, this work does not cover the scope of exploring single-particle imaging within live cells. Ongoing collaborative works in our laboratories involve further modification of particle synthesis and imaging technique to enhance the signal-to-background ratio of single-particle imaging. Results from these studies will be published in the near future.

Conclusions

In summary, we demonstrated that NMMO serves as a stoichiometric ('sacrificial') catalyst to mediate nanoscale surface oxidation of CDs to produce multicolour CDs with single composition. Several groups have previously demonstrated that PL sensitivity can be successfully correlated with their surface chemistry. However, this task is not simple and may require high synthetic control without altering their basic surface properties. Our report for the first time demonstrated that a stoichiometric catalyst can be employed successfully as a single additive to aid nanoscale surface oxidation. As confirmed through MS spectrometry and other analytical means, NMMO is irreversibly consumed in the reaction system to enable production of sub-20 nm particles without compromising brightness or stability. To the best of our knowledge, this report for the first time demonstrated that catalytically-facilitated nanoscale aerial oxidation may lead to highly luminescent CDs when compared with non-catalytic CDs. Such enhanced oxidation causes a six-fold increase in oxidative nanoscale surface and produces stable carbon nanoparticles with a two-fold increase in quantum yield that allows for single-particle imaging. We expect that NMMO-mediated surface oxidation represents a promising strategy to produce brighter carbon nanoparticles suitable for single-particle tracking as well as multiplexed bio-imaging in the near future.

Conflicts of interest

DP is co-founder of three start-up companies that did not support this work.

Acknowledgements

Zeta potential measurements, FT-IR spectroscopy and Raman spectroscopy measurements were performed at Frederick Seitz Materials Research Laboratory. Mass spectroscopy studies and fluorescence EMM measurements at were performed at SCS, UIUC and ISTC, UIUC, respectively. We thank Richard T. Haasch for helping with XPS studies, Dr Iwona Dobrucka for IVIS experiments, John Scott for Fluorescence EMM measurements, and Dr Hannah Walukiewicz for fluorescence measurements. We thank the support from the University of Illinois at Urbana-Champaign.

Notes and references

1 K. Qu, J. Wang, J. Ren and X. Qu, *Chem. – Eur. J.*, 2013, **19**, 7243.
2 Z. Lin, W. Xue, H. Chen and J.-M. Lin, *Anal. Chem.*, 2011, **83**, 8245.
3 H. Nie, M. Li, Q. Li, S. Liang, Y. Tan, L. Sheng, W. Shi and S. X-A. Zhang, *Chem. Mater.*, 2014, **26**, 3104.
4 W. Wei, C. Xu, J. Ren, B. Xua and X. Qu, *Chem. Commun.*, 2012, **48**, 1284.
5 S. Liu, J. Tian, L. Wang, Y. Zhang, X. Qin, Y. Luo, A. M. Asiri, A. O. Al-Youbi and X. Sun, *Adv. Mater.*, 2012, **24**, 2037.
6 S.-T. Yang, L. Cao, P. G. Luo, F. Lu, X. Wang, H. Wang, M. J. Meziani, Y. Liu, G. Qi and Y.-P. Sun, *J. Am. Chem. Soc.*, 2009, **131**, 11308.
7 Y.-P. Sun, B. Zhou, Y. Lin, W. Wang, K. A. S. Fernando, P. Pathak, M. J. Meziani, B. A. Harruff, X. Wang, H. Wang, P. G. Luo, H. Yang, M. K. Kose, B. Chen, L. M. Veca and S.-Y. Xie, *J. Am. Chem. Soc.*, 2006, **128**, 7756.
8 I. Srivastava, S. K. Misra, I. Tripathi, A. Schwartz-Duval and D. Pan, *Adv. Biosyst.*, 2018, **2**, 1800009.
9 S. K. Misra, I. Srivastava, I. Tripathi, E. Daza, F. Ostadhossein and D. Pan, *J. Am. Chem. Soc.*, 2017, **139**, 1746.
10 S. K. Misra, F. Ostadhossein, E. Daza, E. V. Johnson and D. Pan, *Adv. Funct. Mater.*, 2016, **26**, 8031.
11 F. Yi, G. Xiaoyang, Z. Yongqiang, L. Ying, L. Xingyuan, Z. Yongqiang and Z. Jialong, *ACS Appl. Mater. Interfaces*, 2016, **8**, 31863.
12 J. Kai, S. Shan, Z. Ling, L. Yue, W. Aiguo, C. Congzhong and L. Hengwei, *Angew. Chem.*, 2015, **54**, 5360.
13 J. Ge, Q. Jia, W. Liu, L. Guo, Q. Liu, M. Lan, H. Zhang, X. Meng and P. Wang, *Adv. Mater.*, 2015, **27**, 4169.
14 H. Zheng, Q. Wang, Y. Long, H. Zhang, X. Huang and R. Zhu, *Chem. Commun.*, 2011, **47**, 10650.
15 S. K. Misra, H.-H. Chang, P. Mukherjee, S. Tiwari, A. Ohoka and D. Pan, *Sci. Rep.*, 2015, **5**, 14986.
16 (*a*) L. Bao, Z.-L. Zhang, Z.-Q. Tian, L. Zhang, C. Liu, Y. Lin, B. Qi and D.-W. Pang, *Adv. Mater.*, 2011, **23**, 5801.
17 S. Khan, W. Li, N. Karedla, J. Thiart, I. Gregor, A. M. Chizhik, J. Enderlein, C. K. Nandi and A. I. Chizhik, *J. Phys. Chem. Lett.*, 2017, **8**, 5751.

Published on 16 August 2018. Downloaded by University of Illinois - Urbana on 8/23/2018 4:20:31 PM.

18 S. Zhu, Y. Song, X. Zhao, J. Shao, J. Zhang and B. Yang, *Nano Res.*, 2015, **8**, 355.
19 S. Ghosh, A. M. Chizhik, N. Karedla, M. O. Dekaliuk, I. Gregor, H. Schuhmann, M. Seibt, K. Bodensiek, I. A. T. Schaap, O. Schulz, A. P. Demchenko, J. Enderlein and A. I. Chizhik, *Nano Lett.*, 2014, **14**, 5656.
20 S. A. Empedocles, R. Neuhauser and M. G. Bawendi, *Nature*, 1999, **399**, 126.
21 L. E. Brus, P. F. Szajowski, W. L. Wilson, T. D. Harris, S. Schuppler and P. H. Citrin, *J. Am. Chem. Soc.*, 1995, **117**, 2915.
22 A. I. Chizhik, A. M. Chizhik, D. Khoptyar, S. Bär and A. J. Meixner, *Nano Lett.*, 2011, **11**, 1131.
23 T. Schmidt, A. I. Chizhik, A. M. Chizhik, K. Potrick, A. J. Meixner and F. Huisken, *Phys. Rev. B: Condens. Matter Mater. Phys.*, 2012, **86**, 125302.
24 A. M. Chizhik, A. I. Chizhik, R. Gutbrod, A. J. Meixner, T. Schmidt, J. Sommerfeld and F. Huisken, *Nano Lett.*, 2009, **9**, 3239.
25 R. Wang, K.-Q. Lu, Z.-R. Tang and Y.-J. J. Xu, *Mater. Chem. A*, 2017, **5**, 3717.
26 K. Hola, A. B. Bourlinos, O. Kozak, K. Berka, K. M. Siskova, M. Havrdova, J. Tucek, K. Safarova, M. Otyepka, E. P. Giannelis and R. Zboril, *Carbon*, 2014, **70**, 279.
27 H. Ding, S.-B. Yu, J.-S. Wei and H.-M. Xiong, *ACS Nano*, 2016, **10**, 484.
28 T. Gokus, R. Nair, A. Bonetti, M. Bohmler, A. Lombardo, K. Novoselov, A. Geim, A. Ferrari and A. Hartschuh, *ACS Nano*, 2009, **3**, 3963.
29 S. Qu, D. Zhou, D. Li, W. J. Pengtao, J. Dong, H. Lei, L. Haibo and Z. D. Shen, *J. Polym. Sci., Part A: Polym. Chem.*, 2016, **28**, 3516.
30 A. B. Bourlinos, A. Stassinopoulos, D. Anglos, R. Zboril, M. Karakassides and E. P. Giannelis, *Small*, 2008, **4**, 455.
31 D. Pan, *Mol. Pharm.*, 2013, **10**, 781–782.
32 D. Pan, S. D. Caruthers, A. Senpan, C. Yalaz, A. J. Stacy, G. Hu, J. N. Marsh, P. J. Gaffney, S. A. Wickline and G. M. Lanza, *J. Am. Chem. Soc.*, 2011, **133**, 9168.
33 D. Pan, B. Kim, L. V. Wang and G. M. Lanza, *Wiley Interdiscip. Rev.: Nanomed. Nanobiotechnol.*, 2013, **5**, 517.
34 P. Mukherjee, S. K. Misra, M. C. Gryka, H. H. Chang, S. Tiwari, W. L. Wilson, J. W. Scott, R. Bhargava and D. Pan, *Small*, 2015, **11**, 4691.
35 Q. Wang, X. Liu, L. Zhang and Y. Lv, *Analyst*, 2012, **137**, 5392.
36 X. Xu, R. Ray, Y. Gu, H. J. Ploehn, L. Gearheart, K. Raker and W. A. Scrivens, *J. Am. Chem. Soc.*, 2004, **126**, 12736.
37 S.-T. Yang, X. Wang, H. Wang, F. Lu, P. G. Luo, L. Cao, M. J. Meziani, J.-H. Liu, Y. Liu, M. Chen, Y. Huang and Y.-P. Sun, *J. Phys. Chem. C*, 2009, **113**, 18110.
38 J. Lu, J.-x. Yang, J. Wang, A. Lim, S. Wang and K. P. Loh, *ACS Nano*, 2009, **3**, 2367.
39 J. Wang, S. Sahu, S. K. Sonkar, K. N. Tackett Ii, K. W. Sun, Y. Liu, H. Maimaiti, P. Anilkumar and Y.-P. Sun, *RSC Adv.*, 2013, **3**, 15604.
40 H. Li, R. Liu, Y. Liu, H. Huang, H. Yu, H. Ming, S. Lian, S.-T. Lee and Z. Kang, *J. Mater. Chem.*, 2012, **22**, 17470.
41 B. Chen, F. Li, S. Li, W. Weng, H. Guo, T. Guo, X. Zhang, Y. Chen, T. Huang, X. Hong, S. You, Y. Lin, K. Zeng and S. Chen, *Nanoscale*, 2013, **5**, 1967.
42 W. Wang, Y. Ni and Z. Xu, *J. Alloys Compd.*, 2015, **622**, 303.
43 R. Liu, D. Wu, S. Liu, K. Koynov, W. Knoll and Q. Li, *Angew. Chem.*, 2009, **121**, 4668.
44 H. Jiang, F. Chen, M. G. Lagally and F. S. Denes, *Langmuir*, 2010, **26**, 1991.
45 J. H. Park, S. N. Thorgaard, B. Zhang and A. J. Bard, *J. Am. Chem. Soc.*, 2013, **135**, 5258.
46 J. A. Harris, Y. Liu, P. Yang, P. Kner and K. F. Lechtreck, *Mol. Biol. Cell*, 2016, **27**, 295.
47 R. Benhaddou, S. Czernecki, W. Farid, G. Ville, J. Xie and A. Zegar, *Carbohydr. Res.*, 1994, **260**, 243.
48 A. A. Kokorina, E. S. Prikhozhdenko, G. B. Sukhorukov, A. V. Sapelkin and I. Y. Goryacheva, *Russ. Chem. Rev.*, 2017, **86**, 1157.
49 K. Zhang, Y. Osakada, M. Vrljic, L. Chen, H. V. Mudrakola and B. Cui, *Lab Chip*, 2010, **10**, 2566.

 This journal is © The Royal Society of Chemistry 2018